J Mater Sci: Mater Med (2011) 22:253–262
DOI 10.1007/s10856-010-4210-6

A combined experimental and modelling approach to aortic valve viscoelasticity in tensile deformation

Afshin Anssari-Benam · Dan L. Bader · Hazel R. C. Screen

Received: 10 November 2010 / Accepted: 8 December 2010 / Published online: 8 January 2011

Abstract The quasi-static mechanical behaviour of the aortic valve (AV) is highly non-linear and anisotropic in nature and reflects the complex collagen fibre kinematics in response to applied loading. However, little is known about the viscoelastic behaviour of the AV. The aim of this study was to investigate porcine AV tissue under uniaxial tensile deformation, in order to establish the directional dependence of its viscoelastic behaviour. Rate dependency associated with different mechanical properties was investigated, and a new viscoelastic model incorporating rate effects developed, based on the Kelvin-Voigt model. Even at low applied loads, experimental results showed rate dependency in the stress–strain response, and also hysteresis and dissipation effects. Furthermore, corresponding values of each parameter depended on the loading direction. The model successfully predicted the experimental data and indicated a 'shear-thinning' behaviour. By extrapolating the experimental data to that at physiological strain rates, the model predicts viscous damping coefficients of 8.3 MPa s and 3.9 MPa s, in circumferential and radial directions, respectively. This implies that the native AV offers minimal resistance to internal shear forces induced by blood flow, a potentially critical design feature for substitute implants. These data suggest that the mechanical behaviour of the AV cannot be thoroughly characterised by elastic deformation and fibre recruitment assumptions alone.

A. Anssari-Benam · D. L. Bader · H. R. C. Screen (✉)
Medical Engineering Division, School of Engineering and Materials Science, Queen Mary, University of London, Mile End Road, London E1 4NS, UK
e-mail: H.R.C.Screen@qmul.ac.uk

1 Introduction

The aortic valve (AV) serves to prevent retrograde blood flow from the aorta to the left ventricle during each cardiac cycle [1]. Comprised of three morphologically distinct layers called the ventricularis, spongiosa and fibrosa, the AV must withstand tensile, flexural and shear stresses upon opening and closure, for over 3×10^9 cycles in a lifetime [2–4]. Functioning in such a dynamic and repetitive loading environment demands specific mechanical properties and significant fatigue resistance, not associated with other connective tissues [4]. Nonetheless, in some subjects, the native AV is still susceptible to failure, creating a significant demand for prosthetic and bioprosthetic valve replacements [5–8]. To date, an ideal substitute has not been developed [6, 7], and the current solutions exhibit a high failure rate within 5 years of implantation [9, 10]. While haemocompatibility causes a number of complications, many structural failures also occur as a result of incompatible mechanical properties [9, 11, 12]. Characterising the mechanical behaviour of the native AV is thus an important first step towards the successful design of replacement implants, able to withstand physiological loading conditions effectively.

The mechanical behaviour of the AV has been primarily characterised using quasi-static uniaxial loading protocols, which have revealed strong directional dependence in valve mechanical properties [13–15]. More recent studies have employed biaxial loading regimes, as a more realistic representation of physiological loading conditions [1, 3, 16]. These tests have confirmed the anisotropic nature of AV mechanical behaviour, and additionally provided insight into the kinematics of collagen fibres, demonstrating the roles of fibre reorientation and recruitment during loading [3, 17, 18].

However, as with many collagenous connective tissues, the AV exhibits viscoelastic behaviour when subjected to specific loading conditions [13, 19]. This response has often been attributed to the glycosaminoglycan (GAG) component of the extra cellular matrix [20]. Indeed, there is evidence that the GAG rich spongiosa layer acts as a damper, to reduce the impact created by sudden changes in pressure gradient at systole, allowing for relative movement of the ventricularis and fibrosa layers upon valve opening and closure through internal shearing [10, 21, 22]. However, the viscoelastic properties of the AV are generally less well characterised [23]. Important viscoelastic characteristics such as rate dependency in tissue stress–strain response, hysteresis and resilience in loading cycles have not been fully evaluated, and the viscous effects of the AV structural constituents on its mechanical behaviour remain largely unknown. Using a biaxial loading modality to investigate AV viscoelasticity has proven complex, as the fibre kinematics associated with such loading conditions prevent the tissue from exhibiting a full range of viscoelastic responses [19, 23, 24]. In order to establish more insights into the viscoelastic response of AV tissue it is thus beneficial to adopt a uniaxial loading protocol. Furthermore, the majority of AV mechanical tests are performed on experimental equipment limited to loading rates considerably less than the physiological value of 15000%/min [25]. In order to predict behaviour at physiological strain rates, a viscoelastic model must be developed to accommodate the nature of the rate dependency of AV tissue. Such a model, validated over a suitable range of experimental data, would allow extrapolation of the findings to the physiological range.

The present work examines the viscoelastic behaviour of AV specimens subjected to uniaxial tensile deformation, in both the circumferential and radial directions, at a 100-fold range of strain rates. Hysteresis and resilience of the tissue were also examined in separate experiments. A constitutive viscoelastic model has been developed based on the tri-layered structure of the AV, incorporating the deformation rate effects, to investigate AV viscoelasticity and predict its influence at physiological strain rates.

2 Materials and methods

Porcine hearts ($n = 16$) were obtained from mature animals, ranging from 18 to 24 months, within 2 h of slaughter, from a local abattoir. The three AV leaflets were dissected from the aortic root and maintained in Dulbecco's Modified Eagle's Medium (DMEM, Sigma, Poole, UK) at room temperature (25°C). From each leaflet a 5 mm wide circumferential or radial strip was excised from the central (belly) region, as shown in Fig. 1a. This yielded a total of 24 pairs of samples.

The thickness was measured by moving each sample through the beam of a non-contact laser micrometer (LSM-501, Mitotuyo, Japan; resolution = 0.5 μm) and recording values at 1 mm increments. Mean thickness was used to determine the cross sectional area of each sample. The samples were returned to DMEM before performing the experiments. All tests were carried out within 2 h of excision of the tissue strips.

The mechanical tests were performed using a material testing machine (Bionix 100, MTS, Cirencester, UK), fitted with custom designed pneumatic grips each with a corrugated surface, to prevent slippage during the experiments. The initial distance between the grips was set at 10 mm for all test protocols. Prior to the start of each test, a tare load of 0.01 N was applied to the specimens, to establish a consistent zero position. The adjusted distance between the grips was then used as the initial length. Force–elongation data was recorded at a frequency of 20 Hz. During all

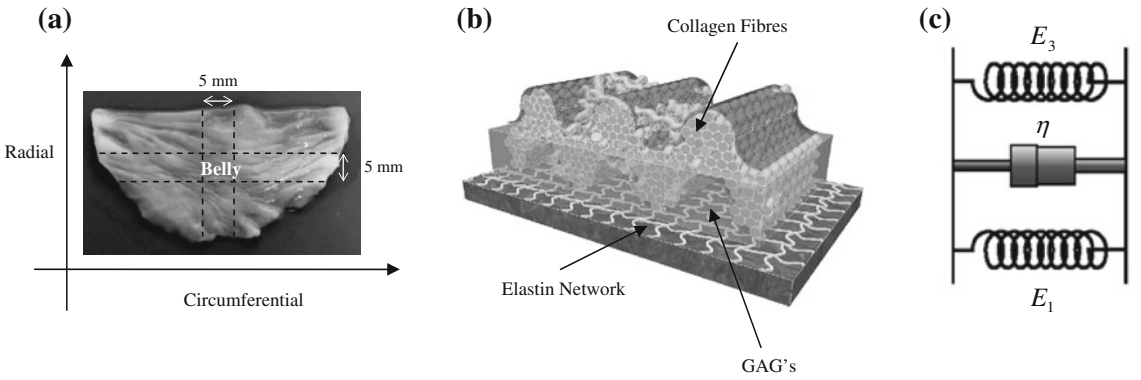

Fig. 1 **a** Image of an AV leaflet from which 5 mm wide strips were cut from the belly region, in either the circumferential or radial direction, **b** schematic diagram of the structural configuration of the AV (adopted from [6]), **c** viscoelastic representation of the AV leaflet with a Kelvin-Voigt model: the ventricularis and fibrosa are modelled with springs with elasticity of E_1 and E_3 respectively, and the spongiosa with a viscous damper with the coefficient of η

mechanical tests, the samples were kept hydrated by spraying with DMEM.

2.1 Uniaxial failure tensile tests

Uniaxial failure tensile tests were carried out at 6%/min, 60%/min, and 600%/min, covering a 100 fold range of strain rates. 12 samples were tested at each rate, 6 loaded circumferentially and 6 radially, and stress–strain curves obtained for each test.

2.2 Incremental one-cycle loading

In order to investigate hysteresis and resilience at different load levels, single cycle tests were performed on both circumferential and radial specimens ($n = 6$ for each group), at a constant strain rate of 60%/min. Successive tests were conducted at incremental levels of pre-defined loads, returning to zero at the end of each cycle, continuing until failure. Samples were loaded to nine different increments, between 5% and 80% of the previously established load at failure (F_{failure}), in the corresponding circumferential and radial directions.

2.3 Viscoelastic model

To model the viscoelastic behaviour of the AV, a constitutive equation of the tri-layered structure was developed using a spring and dashpot configuration, based on a Kelvin-Voigt model (Fig. 1b, c). Here, the two springs represent the elasticity of the ventricularis and fibrosa layers (E_1 and E_3), which are known to be the main load bearing layers within the AV structure [1, 15], while the dashpot represents the spongiosa layer (Fig. 1c). The Green strain and deformation tensors, and the extension ratios used in the model are derived and defined in Appendix 1.

For a Kelvin-Voigt model, the change in the viscoelastic stress tensor from time t_1 to t_2 during deformation can be characterized by superposition of the change in elastic and viscous shear resultants at each time point [26, 27]:

$$\Delta T_{ij}\big|_{t_1}^{t_2} = \Delta T_{ij}^{e} + \Delta T_{ij}^{v}\Big|_{t_1}^{t_2} = \left(T_{ij}^{e} + T_{ij}^{v}\right)_{t_2} - \left(T_{ij}^{e} + T_{ij}^{v}\right)_{t_1} \tag{1}$$

where the indices (i, j) represent the in-plane coordinates, either 1 or 2.

For an arbitrary time of deformation, substitution of the equivalent expressions for T_{ij}^{e} and T_{ij}^{v} in (1) yields:

$$T_{ij} = -P_h\delta_{ij} + E\varepsilon_{ij} + 2\eta V_{ij} \tag{2}$$

where P_h is the hydrostatic pressure that represents the indeterminate part of the stress arising due to the constraint of incompressibility [28], E is the elastic modulus, η is the viscous dissipation coefficient, ε_{ij} is the Green deformation tensor and V_{ij} is the strain rate tensor (Appendix 1). This equation assumes incompressibility [29], as is generally acceptable for biological soft tissues. E is the equivalent elastic element, representing the sum of E_1 and E_3 (Fig. 1c).

The stress tensor components for directions 1 and 2 in (2) will now become:

$$\begin{cases} T_{11} = -P_h + E\varepsilon_{11} + 2\eta V_{11} \\ T_{22} = -P_h + E\varepsilon_{22} + 2\eta V_{22} \\ T_{12} = T_{21} = 0 \end{cases} \tag{3}$$

Substituting for ε_{11} and ε_{22} from Eq. 21 and for V_{11} and V_{22} from Eq. 25 yields:

$$\begin{cases} T_{11} = -P_h + \left(\frac{E}{2}\right)\left(\lambda_1^2 - 1\right) + 2\eta\left(\frac{\dot{\lambda}_1}{\lambda_1}\right) \\ T_{22} = -P_h + \left(\frac{E}{2}\right)\left(\lambda_1^2 - 1\right) + 2\eta\left(\frac{\dot{\lambda}_2}{\lambda_2}\right) \end{cases} \tag{4}$$

Furthermore, in two dimensional analysis, the incompressibility constraint implies that $\lambda_1 \cdot \lambda_2 = 1$, thus T_{22} can be re-written as:

$$T_{22} = -P_h + \left(\frac{E}{2}\right)\left(\lambda_1^{-2} - 1\right) - 2\eta\left(\frac{\dot{\lambda}_1}{\lambda_1}\right) \tag{5}$$

If the continuum experiences a uniaxial tension in direction 1 alone, T_{22} would be zero and thus:

$$P_h = \left(\frac{E}{2}\right)\left(\lambda_1^{-2} - 1\right) - 2\eta\left(\frac{\dot{\lambda}_1}{\lambda_1}\right) \tag{6}$$

Substituting the above equation for T_{11} we get:

$$T_{11} = \frac{E}{2}\left(\lambda_1^2 - \lambda_1^{-2}\right) + 4\eta\left(\frac{\dot{\lambda}_1}{\lambda_1}\right) \tag{7}$$

The change in stress tensor in (1) can thus be rewritten using (7) as:

$$\begin{aligned} \Delta T_{11}\big|_{t_1}^{t_2} = &\left(\frac{E}{2}\left(\lambda_1^2 - \lambda_1^{-2}\right) + 4\eta\left(\frac{\dot{\lambda}_1}{\lambda_1}\right)\right)_{t_2} \\ &- \left(\frac{E}{2}\left(\lambda_1^2 - \lambda_1^{-2}\right) + 4\eta\left(\frac{\dot{\lambda}_1}{\lambda_1}\right)\right)_{t_1} \end{aligned} \tag{8}$$

Setting the initial point of the deformation at $t_1 = 0$, where $\lambda_1 = 1$, the change in stress at time t will thus become:

$$T_{11} = \frac{E}{2}\left(\lambda_1^2 - \lambda_1^{-2}\right) + 4\eta\left(\frac{\dot{\lambda}_1}{\lambda_1}\right) - 4\eta\dot{\lambda}_1 \tag{9}$$

Equation 9 expresses the final form of the viscoelastic model, in the uniaxial tensile deformation. Since the principal directions for the AV leaflet tissue are defined as circumferential and radial, Eq. 9 can be re-written for the two directions as:

$$T_{cir} = \frac{E_{cir}}{2}\left(\lambda_{cir}^2 - \lambda_{cir}^{-2}\right) + 4\eta_{cir}\left(\frac{\dot{\lambda}}{\lambda_{cir}}\right) - 4\eta_{cir}\dot{\lambda} \qquad (10a)$$

and

$$T_{rad} = \frac{E_{rad}}{2}\left(\lambda_{rad}^2 - \lambda_{rad}^{-2}\right) + 4\eta_{rad}\left(\frac{\dot{\lambda}}{\lambda_{rad}}\right) - 4\eta_{rad}\dot{\lambda} \qquad (10b)$$

The inhomogeneous and anisotropic nature of the AV response to tensile deformation necessitates the use of different elastic and damping coefficients in the two orthogonal directions [13, 14, 30], as reflected in the above two Eqs. 10a and 10b.

Equations 10a and 10b were fitted to the experimental stress–strain data sets at each strain rate, for each direction, using the Levenberg–Marquardt algorithm by Origin 8.0 software (Microcal^{TM} Software Inc. USA), for respective parameter estimations.

3 Results

Figure 2 indicates typical stress–strain curves for both circumferential and radial tests to failure, at the three strain rates. It is evident that increasing strain rate leads to an associated increase in failure stress and decrease in failure strain in both the radial and circumferential directions. The mean failure data with standard deviations are compared at each strain rate for both loading directions in Table 1.

Close examination of the typical stress–strain curves at different strain rates (Fig. 2) revealed a sudden transient decrease in stress values in the circumferentially loaded specimens at all strain rates. This decrease (indicated by circles in Fig. 2a) occurred in the second linear region of the σ - ε curves between ε_2 and ε_3. Further inspection highlighted that the decrease occurred between $0.45 < \frac{\sigma_d}{\sigma_f} < 0.6$, where σ_d is the stress at which the decrease occurs and σ_f is the failure stress. No corresponding decrease was observed in the radially oriented specimens.

In order to investigate the extent of non-linearity in the material response under tensile deformation, the tangent modulus E (also referred to as the instantaneous elastic modulus), was numerically estimated from the first derivative of the $\sigma - \varepsilon$ curve at each data point. It was then subjected to smoothing by selecting every 5 data points, a strategy previously adopted by the authors [31]. Typical curves of $E - \varepsilon$, for circumferential and radial samples, at different strain rates are shown in Fig. 3. It is evident that at each strain rate, three distinct regions can be identified, as indicated by the dotted lines in the Figure. These represent:

(1) an initial region in which the modulus is constant (the modulus in this region will be referred to as E_1), implying that the respective $\sigma - \varepsilon$ curve is linear up to a strain of ε_1;
(2) a region in which the value of E increases with the increase in strain, up to a strain of ε_2, resulting in nonlinear behaviour in the respective $\sigma - \varepsilon$ curve; and
(3) a region of constant modulus (referred to as E_3), which results in a second linear section to the $\sigma - \varepsilon$ curve, up to the strain ε_3.

Beyond ε_3, there was a decrease in modulus (Fig. 3), suggesting the initiation of microstructure failure which will subsequently lead to gross specimen failure.

With increasing strain rate, larger values of E were evident in all regions, while the strain range for the initial linear region of the graphs decreased, quantitatively showing that the material becomes stiffer, in both directions. A summary of all mean moduli values in the linear regions (E_1 and E_3), and the respective strain ranges are presented in the Table 1.

Stress-elongation ($\sigma - \lambda$) data were fitted to the model in Eqs. 10a and 10b, for circumferential and radial specimens, respectively. E_{cir} and E_{rad} were determined as $(E_1 + E_3)$, for each loading direction and strain rate (Fig. 3). The corresponding values for η_{cir} and η_{rad} were then estimated using the model. The model provided a good fit, as illustrated in Fig. 4, with the R^2 values in excess of 0.98 for all of the experimental data sets. The values for the two parameters in each direction (E and η) are indicated in Table 2. The model clearly predicts a decrease in damping coefficient with an increase in strain rate for both circumferential and radial directions, indicating a 'shear-thinning' behaviour of the tissue.

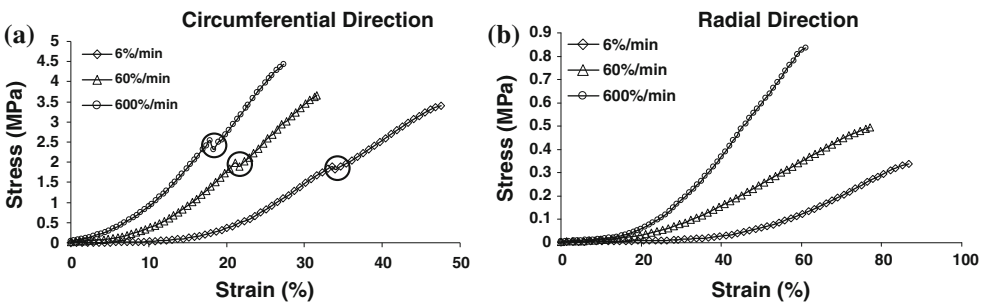

Fig. 2 Typical $\sigma - \varepsilon$ curves for the AV strips loaded at 6%/min, 60%/min and 600%/min, showing: **a** circumferential specimens, and **b** radial specimens. Circles indicate the highly repeatable stress drop in the circumferential direction at all the tested strain rates

Table 1 Values (mean ± SD) of the characteristic mechanical parameters for each of the three regions of the stress–strain curves, evaluated experimentally in both directions and at different rates

Sample	Strain rate (%/min)	UTS (MPa)	Failure strain (%)	E_1 (MPa)	ε_1 (%)	ε_2 (%)	E_3 (MPa)	ε_3 (%)
Circumferential	6	3.44 ± 0.57	45.07 ± 1.25	0.42 ± 0.16	8.05 ± 1.63	28.01 ± 2.61	20.4 ± 0.86	41.25 ± 2.06
	60	3.68 ± 0.12	31.54 ± 1.69	1.63 ± 0.14	4.28 ± 0.88	19.68 ± 2.22	34.07 ± 1.98	28.59 ± 1.77
	600	4.45 ± 0.13	27.56 ± 1.96	4.01 ± 0.42	1.91 ± 0.49	18.69 ± 2.37	37.54 ± 1.45	24.32 ± 1.36
Radial	6	0.34 ± 0.03	87.6 ± 1.78	0.085 ± 0.021	30.8 ± 2.95	64 ± 1.97	0.71 ± 0.8	80.5 ± 2.41
	60	0.50 ± 0.03	77.15 ± 0.03	0.088 ± 0.015	7.73 ± 0.16	44.62 ± 3.2	1.21 ± 0.09	69.11 ± 1.38
	600	0.84 ± 0.05	61.11 ± 0.63	0.15 ± 0.01	6.83 ± 0.04	35.58 ± 1.65	3.36 ± 0.10	58.52 ± 1.24

The indices 1, 2, 3 indicate the first, second and third regions of the stress–strain curves, respectively

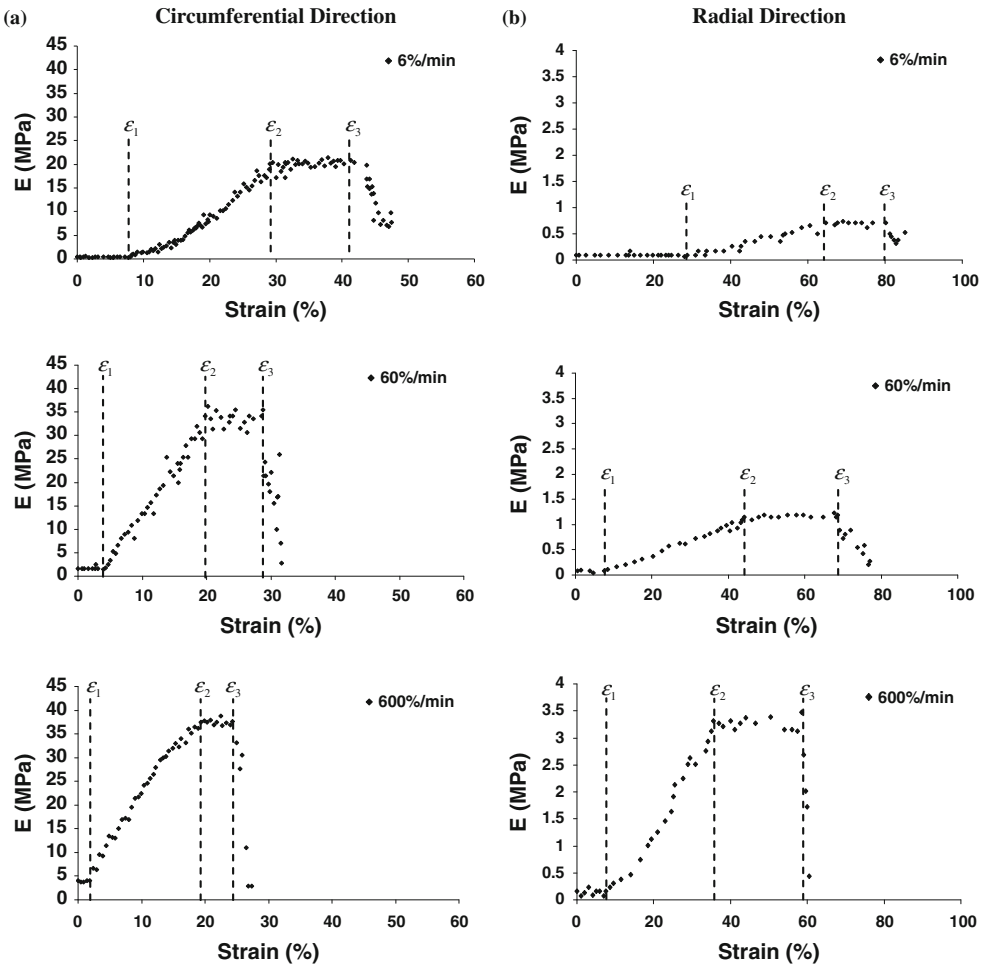

Fig. 3 Typical $E - \varepsilon$ diagrams for the AV strips comparing: **a** circumferential specimens; and **b** radial specimens. The top, middle and bottom panels show the results at 6%/min, 60%/min and 600%/min strain rates, respectively

In order to investigate the hysteresis effects and associated irreversibility, AV specimens were subjected to an incremental one-cycle loading and unloading protocol (Sect. 2.3). Figure 5a and b illustrate the typical resulting force–elongation ($F - \lambda$) curves, where force is described as a percentage of the failure load (F_{failure}). The sudden transient decrease in force in the circumferentially loaded samples was again evident, within the same range as reported in quasi-static tensile tests (Fig. 5a). The ratio of the unloading to loading area was calculated for each cycle, in both loading directions, as shown in Fig. 5c. This ratio, which reflects the degree of specimen resilience, was consistently smaller in the circumferential direction, suggesting less circumferential resilience. In addition, the cycle associated with the sudden decrease in force consistently reported the minimum ratio, suggesting that this phenomenon is contributing to a further reduction of resilience within circumferential specimens.

It has been previously shown that the dissipation of deformation energy will lead to irreversible elongation of

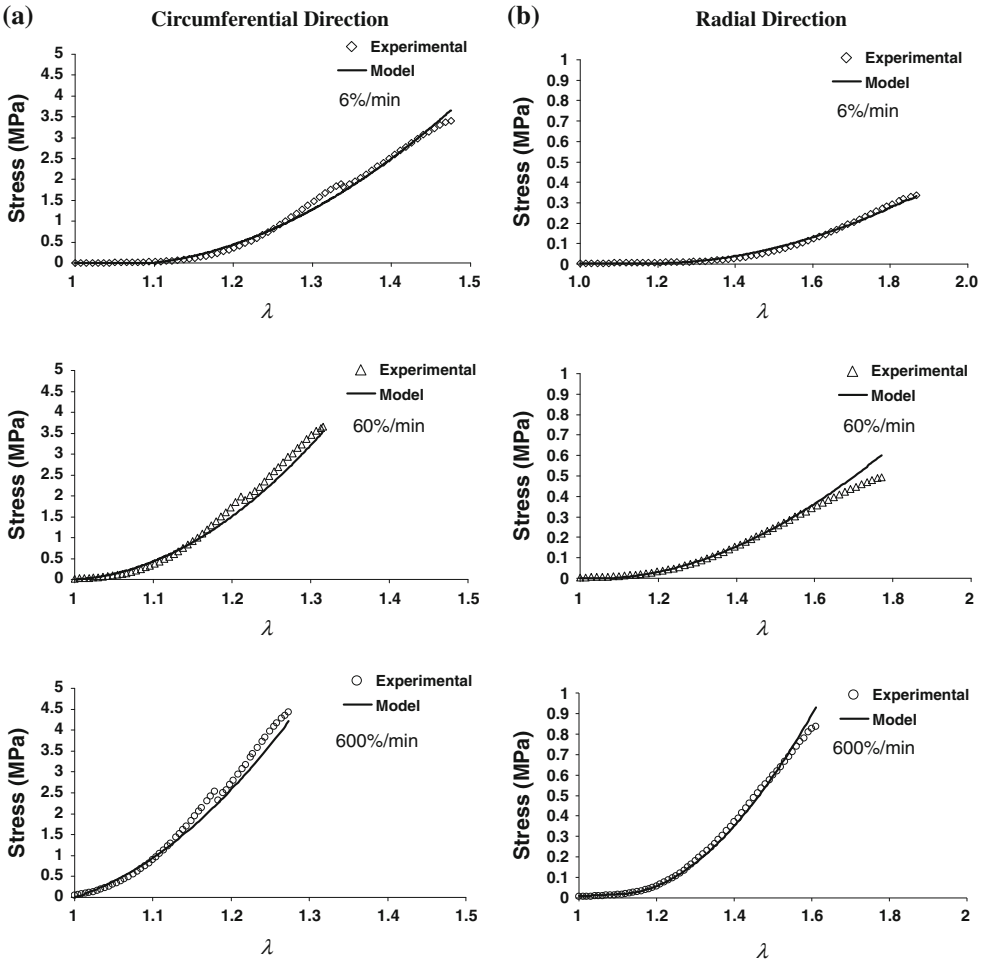

Fig. 4 Typical experimental $\sigma - \lambda$ curves plotted alongside the model (Eq. 10): **a** circumferential specimens; and **b** radial specimens. The top, middle and bottom panels show the curves at 6%/min, 60%/min and 600%/min strain rates respectively

Table 2 The E and η values (mean ± SD) in both directions, at the different strain rates

Strain rate (%/min)	E_{cir} (MPa)	η_{cir} (MPa s)	E_{rad} (MPa)	η_{rad} (MPa s)
6	20.55 ± 2.45	675.06 ± 82.15	0.75 ± 0.28	49.12 ± 3.47
60	35.62 ± 0.97	152.50 ± 6.57	1.26 ± 0.08	6.17 ± 0.37
600	40.84 ± 2.05	18.48 ± 0.99	3.39 ± 0.53	4.59 ± 0.66

the continuum [32]. This could be examined in the present study by relating the percentage change in sample length (estimated from the difference in sample length between the beginning and end of the cycle) to the failure load (Fig. 5d). It can be seen from the figure, that irreversibility of length is present in both loading directions even at small applied loads. The corresponding values are generally higher under circumferential loading.

4 Discussion

This study has examined and quantified the viscoelastic response of the AV under uniaxial tensile deformation, using quasi-static mechanical testing performed at different strain rates. These tests have confirmed the previously reported nonlinear and anisotropic behaviour of the AV [3, 13], with a stiffer response in the circumferential direction, due to the predominantly circumferentially aligned collagen fibres [3, 13]. However, the present data have additionally demonstrated viscous damping effects, rate sensitivity and evidence of hysteresis and irreversibility during loading/unloading cycles, all of which also show dependence on the loading direction.

The $E - \varepsilon$ graphs showed three distinct regions within the non-linear stress–strain response in both loading directions (Fig. 3). The observed differences in the mechanical characteristics of a specimen in each of these

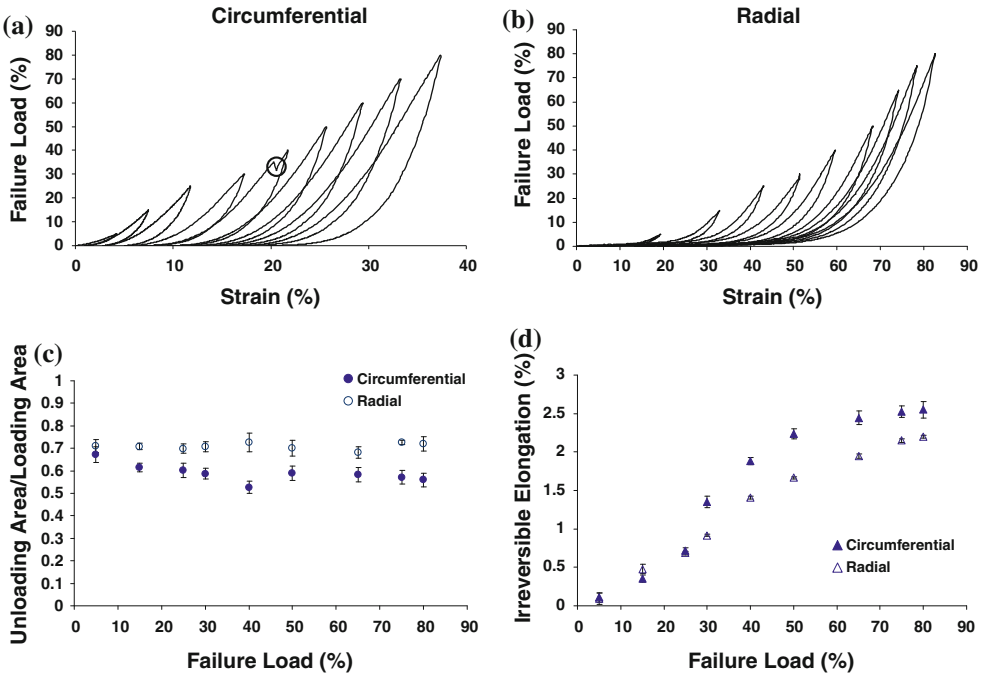

Fig. 5 Hysteresis and recoverability of the AV strips. Typical load-strain curves for the incremental one-cycle loading–unloading tests for: **a** the circumferential; and **b** the radial specimens. **c** recoverability of the specimens (defined as the area underneath the loading divided by the unloading curves) in both directions. **d** irreversible elongation at the loading cycles for both directions

three regions are attributed to the gradual recruitment of collagen fibres, and their increasing role in load bearing within the AV structure [13]. In the initial region of the response, the transmission of tensile force is provided mainly by the elastin component [13], hence the tissue appears to be fairly compliant in nature. However, with increasing applied load, more collagen fibres become recruited and reoriented into the direction of loading. This results in an increase in the tissue stiffness, until the effective volume fraction of the collagen fibres become straightened, by which point the tissue exhibits its maximum stiffness [13].

A repeatable transient decrease in stress was observed in the $\sigma - \varepsilon$ response of the samples loaded circumferentially (Fig. 2). To examine whether this transient decrease was an intrinsic tissue property, and not an artefact arising due to the sample slippage, ink markers were placed on the samples adjacent to the grips and filmed during the tests to failure. Analysis of these videos, using image processing software (ImageJ, NIH), revealed no detectable change of relative marker positions during the tests. Furthermore, the corrugated surface of the grips was altered to reduce the surface friction coefficient, and a number of additional tests carried out. These tests were intended to investigate if the decrease in force would occur earlier than that observed previously, as a result of slippage due to lack of sufficient surface gripping friction. However, in all tests, the decrease repeatedly occurred within the same stress range, implying that it was a direct result of material behaviour in the circumferential direction. Indeed, a similar phenomenon has been reported when testing some other multi-layered collagenous tissues, such as carotid arteries [33], in which the sudden decrease in stress has been attributed to failure of the media layer, prior to the adventitia [33]. Analogous to the arteries, the AV also has two main load bearing layers, the ventricularis and the fibrosa. The ventricularis contains less collagen and more elastin compared to the fibrosa, and is thus likely to fail first at lower stresses, prior to the ultimate failure point of the specimen. The repeated occurrence of this transient decrease in the specific stress range of $0.45 < \frac{\sigma_d}{\sigma_f} < 0.6$ further supports this hypothesis, as it implies that this represents an intrinsic failure parameter of the tissue. Such a decrease was not observed in the radial direction. It is likely that since the collagen fibres are aligned circumferentially, the stiffness of the two layers is more uniform in the radial direction and, as a result, the failure strength of the layers is more closely matched.

A Kelvin-Voigt model was introduced to describe AV viscoelasticity based on the three morphological layers of the valve (Eqs. 10a, 10b). Incorporating the rate effects, the model was seen to provide a good fit to the experimental data at all employed strain rates (Fig. 4), and revealed that the tissue shows 'shear-thinning' behaviour, with reduced effective viscosity at higher strain rates (Table 2). Such behaviour can not be investigated and characterised under elastic deformation assumptions, and has not previously been reported for AV tissue. Nonetheless, a similar trend of behaviour has been observed and reported for concentrated proteoglycan solutions [20]. It seems reasonable to suggest that this behaviour in AV tissue could be attributed to the GAGs associated with the proteoglycans, mainly present within the spongiosa layer [21].

Extrapolating the value of η to a physiological strain rate of 15000%/min would predict values of approximately $\eta_{cir} = 8.3$ MPa s and $\eta_{rad} = 3.9$ MPa s in the circumferential and radial loading directions, respectively. This would imply that the AV tissue offers minimal resistance to internal shear forces induced by blood flow, which constituents a fundamental requirement for any valve replacement. Indeed a material that does not exhibit sufficient shear thinning at physiological loads would markedly increase the shear stresses acting on the leaflet surface. This would inevitably reduce the effective lifetime of the substitute structure and further contribute to complications associated with haemolysis and blood coagulation.

It has previously been shown that the non-linear stress–strain behaviour observed in collagenous soft tissues can be described and modelled by the gradual recruitment of fibres with increasing applied load [34]. However, our model highlights that the constraint of incompressibility, which ensures that strains are coupled in orthogonal directions (Eqs. 4, 5), will also effectively describes the non-linear stress–strain behaviour of the AV, without considering collagen fibre recruitment. This further highlights the complex structure–function relationships in AV mechanical behaviour, suggesting that structural components in addition to the collagen fibre content may contribute to the observed mechanical behaviour.

With respect to the rate dependency, the stress–strain response indicated pronounced rate sensitivity in both directions, with a 100-fold increase in strain rate leading to a 23% increase in mean UTS in the circumferential direction, compared to a 60% increase under radial loading (Table 1). This contrasts with previous studies which have reported negligible rate effects on the mechanical behaviour of the AV tissue [35, 36]. However, this discrepancy may be a result of testing protocols employing a smaller range of strain rates, and may further be exacerbated by the modelling criteria. Indeed some of the well established viscoelastic models, such as quasi-linear viscoelasticity theory (QLV), would only accurately incorporate rate effects if an ideal step or ramp displacement is applied, which is impossible to achieve in experimental protocols [36].

The hysteresis experiments demonstrated greater resilience in samples loaded in the radial than circumferential direction (Fig. 5c), suggesting lower radial dissipative damping effects. These data positively reinforce the modelling calculations, which predicted much lower damping coefficients for radially strained samples (Table 2). Furthermore, it was notable that samples did not show full reversibility in either direction within the time frame of the unloading phase at the prescribed strain rate, which questions the assumption of elastic AV deformation under uniaxial tension, even under low applied loads (Fig. 5c). However, the continual loss of resilience in each cycle might not necessarily imply plastic deformation, but could be attributed to the reorganisation of the AV microstructure during loading/unloading cycles. Microstructural studies are in progress in the host lab to further investigate the response of the microstructural components of AV to the applied mechanical stimuli at a tissue level.

5 Conclusion

The AV demonstrated viscoelastic characteristics under tensile deformation. Stress–strain curves were rate dependant, with enhanced stiffness in both loading directions with increasing strain rates. The development of a new viscoelastic model highlighted the 'shear-thinning' properties of the valve, and also demonstrated that its non-linear behaviour can be described by the coupling of strains in the orthogonal directions, due to the incompressibility of the tissue. The hysteresis cycles showed noticeable dissipation effects, particularly in circumferential direction, producing a degree of irreversibility for each loading cycle. These results further highlight the viscoelastic behaviour of AV tissue when subjected to tensile deformation.

Acknowledgments AAB is funded by a studentship from the UK Engineering & Physical Sciences Research Council (EPSRC). Research was also supported by a Discipline Bridging Initiative (DBI) grant from the EPSRC and Medical Research Council (MRC).

Appendix 1

Let the variables (a_1, a_2, a_3) identify a particle in the original configuration of the continuum, and (x_1, x_2, x_3) be the coordinates of that particle when the body is deformed. The deformation of the body is known if (x_1, x_2, x_3) is a known function of (a_1, a_2, a_3) [29]:

$$x_i = x_i(a_1, a_2, a_3), i = 1, 2, 3 \tag{11}$$

This could mathematically be considered as a transformation from a_1, a_2, a_3 to x_1, x_2, x_3. The transformation is one-to-one, such that is the functions in (11) are single-valued, continuous and have a unique inverse:

$$a_i = a_i(x_1, x_2, x_3) \tag{12}$$

for every point in continuum [29].

Consider an infinitesimal line element connecting the point $P(a_1, a_2, a_3)$ to a neighbouring point $P'(a_1 + da_1, a_2 + da_2, a_3 + da_3)$. The length of the line PP' in the original configuration of the continuum will be:

$$ds_0^2 = da_1^2 + da_2^2 + da_3^2 \tag{13}$$

When P and P' are deformed to the points $Q(x_1, x_2, x_3)$ and $Q'(x_1 + dx_1, x_2 + dx_2, x_3 + dx_3)$, respectively, the length ds of the new deformed QQ' line is:

$$ds^2 = dx_1^2 + dx_2^2 + dx_3^2 \tag{14}$$

From Eqs. 11 and 12 one can get:

$$dx_i = \frac{\partial x_i}{\partial a_j} da_j,\ da_i = \frac{\partial a_i}{\partial x_j} dx_j \tag{15}$$

Considering Eq. 15, Eqs. 13 and 14 can now be written as:

$$ds_0^2 = da_i da_j \delta_{ij} = \frac{\partial a_i}{\partial x_l} \cdot \frac{\partial a_j}{\partial x_m} dx_l dx_m \delta_{ij} \tag{16}$$

$$ds^2 = dx_i dx_j \delta_{ij} = \frac{\partial x_i}{\partial a_l} \cdot \frac{\partial x_j}{\partial a_m} da_l da_m \delta_{ij} \tag{17}$$

where δ_{ij} is the Kronecker delta. Now the following can be written:

$$ds^2 - ds_0^2 = dx_i dx_j \delta_{ij} - da_i da_j \delta_{ij} = \left(\frac{\partial x_l}{\partial a_i} \cdot \frac{\partial x_k}{\partial a_j} - \delta_{ij} \right) da_i da_j \tag{18}$$

The Green strain tensor is defined by the term in parenthesis in the above equation as [29]:

$$\varepsilon_{ij} = \frac{1}{2} \left(\frac{\partial x_l}{\partial a_i} \cdot \frac{\partial x_k}{\partial a_j} - \delta_{ij} \right) \tag{19}$$

Defining the extension ratios in the principle planar directions of 1 and 2 by λ_1 and λ_2, as the ratio of the final length of the element to its original length, we will have:

$$\lambda_1 = \frac{\partial x_1}{\partial a_1},\ \lambda_2 = \frac{\partial x_2}{\partial a_2} \tag{20}$$

Now the components of the Green strain tensor in Eq. 19 for deformation in directions 1 and 2 can be written by the extension ratios in Eq. 20 as:

$$\begin{cases} \varepsilon_{11} = \dfrac{(\lambda_1^2 - 1)}{2} \\ \varepsilon_{22} = \dfrac{(\lambda_2^2 - 1)}{2} \\ \varepsilon_{12} = \varepsilon_{21} = 0 \end{cases} \tag{21}$$

Taking the time derivative of Eq. 18 gives the rate of deformation tensor in terms of the time rate of Green strain tensor:

$$\left[\left(\frac{\partial v_i}{\partial x_j} \right) + \left(\frac{\partial v_j}{\partial x_i} \right) \right] dx_i dx_j = 2 \dot{\varepsilon}_{ij} da_i da_j \tag{22}$$

where v_i is the ith component of the in-plane velocity field, x_i, and the rate of deformation tensor would be:

$$V_{ij} = \frac{1}{2} \left[\left(\frac{\partial v_i}{\partial x_j} \right) + \left(\frac{\partial v_j}{\partial x_i} \right) \right] \tag{23}$$

For an arbitrary choice of coordination component, and considering Eq. 22, the above equation becomes:

$$V_{ij} = \dot{\varepsilon}_{kl} \left(\frac{\partial a_k}{\partial x_i} \right) \left(\frac{\partial a_l}{\partial x_j} \right) \tag{24}$$

From Eqs. 21 and 24, the components of the rate of deformation tensor in directions 1 and 2 can be obtained as:

$$\begin{cases} V_{11} = \dfrac{\dot{\lambda}_1}{\lambda_1} \\ V_{22} = \dfrac{\dot{\lambda}_2}{\lambda_2} \\ V_{12} = V_{21} = 0 \end{cases} \tag{25}$$

References

1. Stella JA, Sacks MS. On the biaxial mechanical properties of the layers of the aortic valve leaflet. J Biomech Eng. 2007;129:757–66.
2. Brewer RJ, Mentzer RM, Deck JD, Ritter RC, Trefil JS, Nolan SP. An in vivo study of the dimensional changes of the aortic valve leaflets during the cardiac cycle. J Thorac Cardiovasc Surg. 1977;74:645–50.
3. Billiar KL, Sacks MS. Biaxial mechanical properties of the natural and glutaraldehyde treated aortic valve cusp—part I: experimental results. J Biomech Eng. 2000;122:23–30.
4. Merrymanm WD, Youn I, Lukoff HD, Krueger PM, Guilak F, Hopkins RA, Sacks MS. Correlation between heart valve interstitial cell stiffness and transvalvular pressure: implications for collagen biosynthesis. Am J Physiol Heart Circ Physiol. 2006; 290:H224–31.
5. Yacoub MH, Cohn LH. Novel approaches to cardiac valve repair: from structure to function: part I. Circulation. 2004;109:942–50.
6. Vesely I. Heart valve tissue engineering. Circ Res. 2005;97:743–55.
7. Schoen FJ, Levy RJ. Calcification of tissue heart valve substitute: progress toward understanding and prevention. Ann Thorac Surg. 2005;79:1072–80.
8. Lloyd-Jones D, Adams RJ, Brown TM, et al. Heart disease and stroke statistics 2010 update: a report from the American Heart Association. Circulation. 2010;121:e46–215.
9. De Hart J. Fluid-structure interaction in the aortic heart valve. Ph.D. thesis. 2002; Eindhoven University of Technology, Eindhoven, Netherlands.
10. Schoen FJ, Levy RJ. Tissue heart valves: current challenges and future research perspectives. J Biomed Mater Res. 1999;47: 439–65.
11. Jamieson WR. Modern cardiac valve devices-bioprostheses and mechanical prostheses: state of the art. J Cardiac Surg. 1993;8: 89–98.
12. Schoen FJ, Levy RJ, Piehler HR. Pathological considerations in replacement cardiac valves. Cardiovasc Pathol. 1992;1:29–52.
13. Sauren AAHJ, Van Hout MC, Van Steenhoven AA, Veldpaus FE, Janssen JD. The mechanical properties of porcine aortic valve tissues. J Biomech. 1983;16:327–37.
14. Mavrilas D, Missirlis Y. An approach to the optimization of preparation of bioprosthetic heart valves. J Biomech. 1991;24: 331–9.

15. Vesely I. The role of elastin in aortic valve mechanics. J Biomech. 1998;31:115–23.
16. Christie GW, Barratt-Boyes BG. Biaxial mechanical properties of explanted aortic allograft leaflets. Ann Thorac Surg. 1995;60: S160–4.
17. Billiar KL, Sacks MS. Biaxial mechanical properties of the natural and glutaraldehyde treated aortic valve cusp—part II: a structural constitutive model. J Biomech Eng. 2000;122:327–35.
18. Chong M, Missirlis YF. Aortic valve mechanics part II: a stress analysis of the porcine aortic valve leaflets in diastole. Biomat Med Dev Art Org. 1978;6:225–44.
19. Stella JA, Liao J, Sacks MS. Time dependent biaxial mechanical behaviour of the aortic heart valve leaflet. J Biomech. 2007;40: 3169–77.
20. Ratcliffe A, Mow VC. Articular cartilage. In: Comper WD, editor. Extracellular matrix, vol. 1. Amsterdam: Harwood Academic Publishers; 1996. p. 268–72.
21. Brody S, Pandit A. Microarchitectural characterization of the aortic heart valve. In: Hasirci N, Hasirci V, editors. Biomaterials: from molecules to engineered tissues. Kluwer Academic/Plenum Publishers; 2004. p. 167–86.
22. Talman EA, Boughner DR. Internal shear properties of fresh porcine aortic valve cusps: Implications for normal valve function. J Heart Valve Dis. 1996;5:152–9.
23. Sacks MS, Merryman WD, Schmidt DE. On the biomechanics of heart valve function. J Biomech. 2009;42:1804–24.
24. Liao J, Yang L, Grashow J, Sacks MS. The relation between collagen fibril kinematics and mechanical properties in the mitral valve anterior leaflet. J Biomech Eng. 2007;129:78–87.
25. Leeson-Dietrich J, Boughner D, Vesely I. Porcine pulmonary and aortic valves: a comparison of their tensile viscoelastic properties at physiological strain rates. J Heart Valve Dis. 1995;4:88–94.
26. Love ER. Linear superposition in visco-elasticity and theories of delayed effects. Austral J Phys. 1952;9:1–12.
27. Drapaca CS, Tenti G, Rohlf K, Sivaloganathan S. A quasi-linear viscoelastic constitutive equation for the brain: application to hydrocephalus. J Elast. 2006;85:65–83.
28. Pioletti DP, Rakotomanana LR, Benvenuti JF, Leyvraz PF. Viscoelastic constitutive law in large deformations: application to human knee ligaments and tendons. J Biomech. 1998;31:753–7.
29. Fung YC. Biomechanics: mechanical properties of living tissue. 2nd ed. New York: Springer-Verlag New York Inc.; 1993.
30. Li J, Luo XY, Kuang ZB. A nonlinear anisotropic model for porcine aortic heart valves. J Biomech. 2001;34:1279–89.
31. Screen HRC, Lee DA, Bader DL, Shelton JC. An investigation into the effects of the hierarchical structure of tendon fascicles on micromechanical properties. Proc Insts Mech Engrs Part H: J Eng Med. 2004;218:109–19.
32. Anssari-Benam A, Viola G, Korakianitis T. Thermodynamic effects of linear dissipative small deformations. J Therm Anal Calorim. 2010;100:941–7.
33. Teng Z, Tang D, Zheng J, Woodard PK, Hoffman AH. An experimental study on the ultimate strength of the adventitia and media of human atherosclerotic carotid arteries in circumferential and axial directions. J Biomech. 2009;42:2535–9.
34. Lanir Y. Constitutive equations for fibrous connective tissues. J Biomech. 1983;16:1–12.
35. Rousseau EPM, Sauren AAHJ, Van Hout MC, Van Steenhoven AA. Elastic and viscoelastic material behaviour of fresh and glutaraldehyde-treated porcine aortic valve tissue. J Biomech. 1983;16:339–48.
36. Doehring TC, Carew EO, Vesely I. The effect of strain rate on the viscoelastic response of aortic valve tissue: a direct-fit approach. Ann Biomed Eng. 2004;32:223–32.